Microstructures and lattice preferred orientations in experimentally deformed clinopyroxene aggregates

A. Mauler[a], M. Bystricky[a], K. Kunze[a,*], S. Mackwell[b]

[a]*Geologisches Institut, ETH-Zentrum, CH-8092 Zürich, Switzerland*
[b]*Bayerisches Geoinstitut, Universität Bayreuth, D-95440 Bayreuth, Germany*

Abstract

Microstructures and lattice preferred orientations (LPO) were analysed on experimentally deformed natural and hot-pressed clinopyroxene aggregates in order to understand the relationship between deformation processes and evolving microstructures. The LPO was measured using electron backscatter diffraction techniques in the scanning electron microscope (SEM). Microstructures were observed by polarized light microscopy and by orientation contrast in the SEM. Natural samples (Sleaford Bay pyroxenite) were deformed in axial compression stepping tests up to 16% shortening. These samples deformed mainly by twinning and dislocation glide with very little recrystallization. No clear LPO evolution apart from the initial LPO could be attributed to deformation. Synthetic clinopyroxenite samples were hot-pressed from powders of the same material with three different grain size ranges, and deformed in compression stepping experiments up to 28% shortening. In the samples with coarse (30 μm) and intermediate (20 μm) grain sizes, deformation was dominated by dislocation creep accommodated by subgrain rotation recrystallization. The recrystallized grains have sizes up to 8 μm and represent 15–25% of the sampled area. The sample with the finest initial grain size (5 μm) deformed dominantly by diffusion creep accompanied by grain boundary migration. All of the hot-pressed samples deformed in compression have a similar texture, consisting of a girdle of **c**[001] axes normal to compression and a point maximum of **b**[010] axes and **a***(100) poles parallel to the compression direction. The LPO of recrystallized grains was separated on spatially resolved orientation maps and shows an S-type fabric with **b**[010] parallel to the compression axis and a random **a***(100) distribution. The bulk fabric was largely present in the hot-pressed starting material and is interpreted as the result of compaction during cold-pressing. At moderate strains in axial compression, the initial compaction fabric has been weakly overprinted by the recrystallization fabric. One hot-pressed sample (coarse grain size) was deformed in torsion to a shear strain of $\gamma = 0.1$. The microstructure indicates dominant dislocation creep and contains about 20% recrystallized grains. The texture evolved from the rotationally symmetric compaction LPO to an oblique fabric. © 2000 Elsevier Science Ltd. All rights reserved.

1. Introduction

Although single-phase clinopyroxenites are not a common rock type in the earth's crust or mantle, clinopyroxene can locally control the rheological behavior and physical properties of rocks such as eclogites and gabbros where it occurs in high proportions. Owing to the high anisotropy in the physical properties of single crystal clinopyroxene, the development of lattice preferred orientations (LPO) in clinopyroxene may influence the bulk anisotropy of such rocks significantly.

In the LPO patterns most commonly observed in natural clinopyroxene, **c**[001] is preferentially oriented parallel to the lineation while **b**[010] is normal to the foliation plane. This pattern varies with the axis ratios of the shape fabric ellipsoid (Godard and Van Roermund, 1995). In strongly lineated samples, the maximum of **c**[001] forms a point maximum parallel to the lineation and **b**[010] spreads out in a great circle normal to the lineation (L-type fabric of Helmstaedt et al., 1972). In strongly foliated samples, the maximum of **b**[010] describes a point maximum normal to the foliation plane, while **c**[001] is dispersed within the foliation plane (S-type fabric of Helmstaedt et al., 1972). However, the development of these fabrics is not satisfactorily explained by dislocation glide only on the known slip systems (see below). The S- and L-type preferred orientations would correspond to 'easy slip' on (010) **c**[001], which has not been reported as a dominant slip system by transmission electron microscopy (TEM) observations. Therefore, other mechanisms have recently been used to interpret these fabrics, such as grain boundary migration and diffusive mass transfer (Godard and Van Roermund, 1995). In omphacite, a temperature-dependent switch in dominant slip systems due to a space group transformation

Fig. 1. Stereogram of diopside with main slip planes and directions marked. (Upper hemisphere equal area projection.)

was discussed as the cause of the L- to S-type transition (Brenker, 1998; Brenker et al., 1999).

Through extensive TEM investigations on experimentally deformed diopside single crystals and polycrystalline aggregates, two intracrystalline deformation regimes have been recognized in clinopyroxene. At low temperatures and high strain rates, plastic strain is accommodated by mechanical twinning on (100) [**c**] and (001) [**a**] and by dislocation glide on the (100) [**c**] slip system (Raleigh and Talbot, 1967; Avé Lallemant, 1978; Kollé and Blacic, 1983; Kirby and Kronenberg, 1984; Boland and Tullis, 1986). At high temperatures (T > 500°C), multiple slip occurs involving the slip systems (100) [**c**], {110} $\frac{1}{2}$<**a** ± **b**>, {110} [**c**], (010) [**a**], (100) [**b**] and (010) [**a** + **c**] (Boland and Tullis, 1986; Ingrin et al., 1992). According to Ingrin et al. (1991) and Raterron et al. (1994), (100) [**c**] is the easiest slip system at intermediate temperature, while {110} $\frac{1}{2}$<**a** ± **b**> and {110} [**c**] dominate at high temperature (T ≥ 800°C). The crystallographic planes and directions of the slip systems in diopside are represented in Fig. 1.

There have been few experimental studies on pure polycrystalline clinopyroxenites (Carter et al., 1972; Etheridge and Kirby, 1977; Kirby and Christie, 1977; Kirby and Kronenberg, 1984; Boland and Tullis, 1986). Only two of them reported LPO measurements. Carter et al. (1972) measured the LPO of a hot-pressed sample of polycrystalline diopside deformed in compression. The sample was characterized by significant recrystallization and grain growth. The **b**[010] axes align parallel to the compression axis σ_1 and **a**[100] and **c**[001] axes form girdles with maxima in the $\sigma_2 = \sigma_3$ plane. Etheridge and Kirby (1977) performed compression experiments on clinopyroxene aggregates at constant strain rates. No clear LPO development was identified after 45% strain. Thus, microstructures

and LPO have not been intensively documented, although they are an important link for comparison of deformation mechanisms in naturally and experimentally deformed clinopyroxenes.

Sleaford Bay pyroxenite, composed predominantly of Fe-rich diopside, has previously been used as a starting material for deformation experiments (Kirby and Christie, 1977; Kirby and Kronenberg, 1984; Boland and Tullis, 1986). Diopside is considered as an analogue for other clinopyroxenes such as omphacite, which have similar crystal structures and space groups (C2/c and P2/n). In this study, we explore the microstructural and LPO evolution in experimentally deformed aggregates derived from Sleaford Bay pyroxenite.

Samples deformed in stepping experiments under uniaxial compression were available from a recent rheological study on the deformation of natural and hot-pressed clinopyroxenite (Bystricky, 1998). Coarse-grained samples (grain size 330 μm) of natural Sleaford Bay pyroxenite were deformed in the dislocation creep regime. Tests on fine-grained samples, prepared by hot-isostatic pressing of selected powders of the same material (grain sizes 5, 20 and 30 μm), allowed the investigation of the transition between dislocation and diffusion creep regimes. Compression tests with similar amounts of finite strain have resulted in clear LPO developments in rocks composed of calcite (Schmid et al., 1980; Wenk, 1985; Rutter et al., 1994) and quartz (Dell'Angelo and Tullis, 1986). Textures of olivine rocks deformed in stepping tests under uniaxial compression were studied recently by Fliervoet et al. (1999).

The microstructural evolution with high shear strains can be studied in samples deformed in torsion. We performed a torsion experiment at constant twist rate (no stepping) on a hot-pressed diopside aggregate to investigate the effects of non-coaxial deformation and, potentially, of higher finite strain on microstructural development.

Throughout this paper, the terms 'dislocation creep' and 'diffusion creep' will be used for the sake of simplicity to refer to the dominant flow regime with a non-linear or linear viscosity, respectively. In a power law relation between strain rate and differential stress, the stress exponent n is equal to one for linear viscous flow and is interpreted to indicate diffusion creep, while n larger than one (typically three to five) is taken to indicate dislocation creep.

2. Analytical techniques

LPOs of diopside were measured using SEM-based electron backscatter diffraction (EBSD) (Venables and Harland, 1973). This technique enables automated determination of the full crystallographic orientation of grains on the surface of a polished sample with spatial resolution of about 1 μm and an absolute angular resolution of 1–2° (Adams et al., 1993; Kunze et al., 1993). In addition, the concurrent use of backscatter and forescatter electron detectors provides

Table 1
Texture index J and extrapolated texture index J_∞ for the analysed samples using various smoothing widths of 5°, 10°, 15° and 30°

	Smoothing width	Natural samples			Hot-pressed samples						
		PI-0	PI-583	PI-592	HP-11	HP-12	PI-527	PI-528	PI-588	PI-598	P0-228
J	5°	95.60	86.54	90.48	14.01	17.10	14.16	12.57	12.42	13.40	13.48
J_∞		56.68	51.32	51.73	2.59	3.15	2.52	2.86	1.99	2.40	3.45
J	10°	14.37	16.60	17.84	3.18	3.38	3.27	3.04	3.23	3.00	3.15
J_∞		9.06	11.66	12.42	1.67	1.40	1.62	1.71	1.73	1.42	1.83
J	15°	5.03	6.04	6.80	1.92	1.84	1.93	1.85	2.10	1.78	1.87
J_∞		3.47	4.49	5.23	1.52	1.26	1.42	1.44	1.64	1.28	1.53
J	30°	1.55	1.73	1.92	1.36	1.22	1.35	1.32	1.50	1.27	1.30
J_∞		1.35	1.50	1.70	1.35	1.15	1.27	1.25	1.43	1.18	1.30

simultaneous phase and orientation contrast imaging, deduced from atomic number contrast and from the electron channelling effect, respectively (Prior et al., 1996).

From the deformed natural samples, polished thin sections parallel to the compression direction were prepared without cover and lapped using a colloidal silica suspension with a particle size of 25 nm for 1 h. The same preparation technique did not provide a well-polished surface for the hot-pressed samples owing to the fine grain size. Therefore, the cylindrical bulk samples were mounted in Plexiglas, mechanically polished and lapped using the same colloidal silica suspension for 4–6 h. All samples were coated with a thin carbon layer (about 3 nm) to reduce specimen charging.

EBSD patterns were collected using a SEM CamScan CS44LB at ETH Zürich with an accelerating voltage of 15 kV and a beam current of approximately 2.5 nA. They were indexed using the software OIM 2.0 (TSL Inc.) on a SGI Indy workstation and a reference file of 40 reflections optimized for omphacite (Mauler et al., 1998). Omphacite is a solid solution of diopside and jadeite with very similar crystal structures. Therefore, the same reflection table was applied with confidence along the solid solution (Mauler, 2000).

For the natural samples, orientation data were collected on a 6000 × 5400 μm square grid with a step size of 60 μm resulting in 9191 measurements. This raster size was chosen to cover as much area of the smallest section as possible, while the step size was small enough to resolve some intra-granular structure. In the synthetic samples, patterns were collected in the middle of the samples on an 800 × 1000 μm grid with a step size of 20 μm (2091 data points). This step size is of the same order as the grain size of the studied samples and gave good sampling statistics, while avoiding duplicate measurements in the same grains. A fine-scale orientation map was obtained on a synthetic sample with a step size of 2 μm on an area 180 × 250 μm. Every measurement on the grid was assigned a confidence index (CI) between 0 and 1 to express the reliability of the EBSD pattern indexing. Orientations with CI < 0.2 are considered to be unreliable and therefore filtered out for density calculations.

Pole figures were obtained from the discrete orientation data using the software package Beartex (Wenk et al., 1998). The orientation distribution function (ODF) was calculated from the reliable orientations (CI > 0.2) by Gaussian convolution using a smoothing width of 30°, defined as the full width at half maximum of a Gaussian bell curve. This value is higher than generally used (10–15°) in order to suppress intentionally any detail in the distributions with finer than 30° angular resolution. For the natural samples, about 400 different grains were covered, which is much less than the total number of EBSD measurements (about 20–25 measurements per grain). If the 400 grains were randomly distributed in orientation space (monoclinic crystal and triclinic sample symmetry), their average orientation distance would be about 33°. Any detail finer than this resolution must be considered purely statistical noise and should be filtered out. To be consistent, the same smoothing width was also applied to the hot-pressed samples, although their counting statistics (1500 grains) would allow a higher angular resolution of 21°.

The strength of the texture is expressed by the texture index J calculated as the mean square value of the ODF (Bunge, 1982). Since J varies with the (finite) number N of individual orientation measurements, the texture strength was also determined as the linear extrapolation (J_∞) of J versus $1/N$ as N goes to infinity (Matthies and Wagner, 1996) for various amounts of smoothing (Viola, 2000). In general, the indices (and the pole densities) increase with decreasing smoothing width, and would diverge to infinity for any discrete data set without smoothing. The differences between J and J_∞ give a measure for the statistical significance of the derived orientation distributions and their errors (Table 1). For the natural samples, high indices of sharp distributions for narrow smoothing up to 15° decrease remarkably for a width of 30°. For the hot-pressed samples, stable indices are available for a smoothing width around 15°. In both cases, the pole figures presented with 30° smoothing contain mainly the statistically sound information, where counting artifacts are suppressed, but appear to be weak compared to common LPO patterns.

For grain size determinations, digitized line drawings of optical photomicrographs (natural samples) and SEM orientation contrast images (hot-pressed samples) were processed
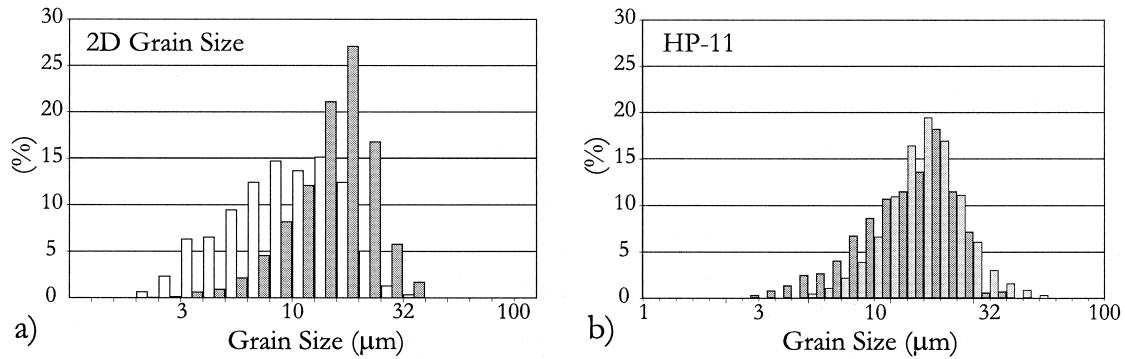
Fig. 2. Comparison of grain size determinations from microstructure and powder for sample HP-11. (a) 2D grain size histogram obtained from microstructural image analysis and expressed as number fraction (white) and area fraction (dark grey) on logarithmic scale. (b) 2D grain size histograms (area fraction) from the microstructure (dark grey) and from powder measurements (light grey), the latter obtained through scaling of the 3D volume fractions by a factor of 1/1.5.

using the public domain program NIH Image version 1.59. Grain sizes were calculated from the measured areas on the binary images, defining the 2D grain size to be equal to the diameter of a circle with the same area.

3D grain sizes of the powders used during sample synthesis were available from laser particle-size analysis (Bystricky, 1998). A comparison between the 3D powder grain sizes and the 2D grain sizes obtained from digitized grain boundaries was performed on hot-pressed sample HP-11. About 80% of the grains on a 2D section fall between 5 and 16 μm and the average is 9 μm (Fig. 2a). This average is at the lower bound of the range (10–30 μm) for the grain size determined from the powder because no 3D correction was applied to our 2D results. To a first approximation, the 2D sectioning effect can be corrected by a constant factor of about 1.5 on the 2D grain sizes (Underwood, 1970). When this correction is applied to the 3D powder data to simulate a 2D distribution, the sizes from powder and microstructural analysis agree very well (Fig. 2b). More precisely, both distributions have their peaks at similar sizes, but the 2D histogram from the microstructure is asymmetric with a tail towards smaller grain sizes. This is expected, since the 3D symmetric 'Gaussian' distribution should project onto an asymmetric 2D histogram with a left-hand tail. Throughout this paper, the 2D grain sizes are given without any 3D correction.

3. Deformation experiments

3.1. Sample preparation

Natural samples were cored in a high purity clinopyroxenite from the Precambrian metamorphic terrain of Sleaford Bay, South Australia. The bulk composition of the clinopyroxenite is $Ca_{0.97}Mg_{0.79}Fe_{0.19}Si_{1.998}O_6$ with trace amounts of Mn, Al, P and Na, as determined by inductively coupled plasma spectrophotometry. About 5% of quartz and <1% of apatite are distributed along grain boundaries and at grain junctions.

Synthetic samples were hot-pressed from powders of the same clinopyroxenite. Three powders of different grain size ranges were obtained after crushing and grinding. Gravitational settling techniques were used to separate powders with the grain size ranges 20–40 μm, 10–30 μm and 1–10 μm as measured with a laser particle-size analyser. The powders were dried for at least 10 h at 1000°C and room pressure with the oxygen fugacity kept near the Ni/NiO buffer by an appropriate mixture of CO/CO_2 gases. Samples were cold-pressed at a uniaxial stress of 150–175 MPa and were hot-isostatically pressed (HIP) in an internally heated gas-medium vessel at 300 MPa confining pressure and 1150–1180°C for ∽ 8 h.

3.2. Compression experiments

All compression experiments were performed in a Paterson gas-medium apparatus located at the University of Minnesota. Prior to deformation, all the samples were dried at 1000°C for 10 h in a controlled-atmosphere furnace. Experiments were carried out under constant load at confining pressures of 300–430 MPa, temperatures of 1150–1225°C and either Ni/NiO or Fe/FeO buffering conditions. Each sample underwent several creep steps at different temperatures, stresses and strain rates (Table 2).

The two natural samples, PI-583 and PI-592, deformed in the dislocation creep regime. A stress exponent n of 4.7 was determined from the stepping experiments. Both samples deformed to a total strain of about 15%. The assembly of sample PI-592 showed a small offset of the pistons, indicating a slight shear component perpendicular to the compression axis in that sample.

The hot-pressed samples were deformed near the transition between dislocation and diffusion creep. The samples underwent various complex deformation histories intended to determine the flow parameters for both creep regimes. From these experiments, stress exponents of 1 and 4.7 were determined for the diffusion and dislocation creep regimes, respectively.

Hot-pressed samples PI-527 and PI-528 had a coarse

Table 2

Compression test conditions for the samples presented in this study. For each temperature, several creep steps were performed in which the flow stress varied within the given ranges. The grain size of the hot-pressed samples after deformation is split into the size of the old coarse grains (P) and the recrystallized fine grains (Rec).

Sample	Starting 2D grain size (μm)	Confining pressure (MPa)	Temperature (°C)	Flow stress (MPa)	Strain rate (10^{-7} s^{-1})	Total strain (%)	Oxygen buffer	Final 2D grain size (μm)
PI-583	330	400	1200	217–383	5–100	5.4	Ni/NiO	330
			1225	223–379	20–210	11.5		
			1175	334–372	25–40	13.2		
			1200	371	100	14.2		
			1225	323	120	15		
PI-592	330	300	1250	169–276	20–220	8.3	Ni/NiO	330
			1200	238–307	10–40	13.1		
			1250	238–278	100–240	15.9		
PI-527	30	300	1200	72–266	50–900	7.9	Ni/NiO	15–40 (P)
			1150	143–293	20–120	15.4		3–8 (Rec)
			1175	116–290	30–260	20.7		
			1225	102–225	190–1250	27.8		
PI-528	30	300	1150	174–300	10–35	3.7	Fe/FeO	15–40 (P)
			1200	134–256	25–100	8.6		2–8 (Rec)
		430	1200	231–383	60–300[a]	14.5		
		300	1225	115–270	60–380[a]	18.8		
PI-588	20	300	1225	50–256	80–920	8.5	Fe/FeO	8–25 (P)
			1200	64–253	25–250	17		3–8 (Rec)
			1150	215–251	20–35	19.7		
			1175	190–277	30–75	22.5		
			1200	190–232	75–100	24.5		
PI-598	5	300	1150	162–261	20–40	5.3	Ni/NiO	2–12
			1200	32–187	20–140	13.4		
			1150	136–220	5–10	17.2		
P0-228	30	300	1200	380	1100	0.1 γ	Ni/NiO	15–40 (P)
								3–8 (Rec)

[a] The apparently low strain rates associated with high differential stresses are due to inhomogeneous deformation of the sample. While part of the cylinder actually deformed to a higher total strain, the strain rate calculations give average values over the whole length of the cylinder.

initial grain size (30 μm). As a result of fracture after hot-pressing, PI-527 deformed inhomogeneously, with one part more deformed than the other and with the development of a high density of microcracks. Homogeneous deformation without cracking was possible for sample PI-528 owing to a higher confining pressure even at the higher differential stresses applied. In both samples, creep data indicate the predominance of dislocation creep.

Hot-pressed samples PI-588 and PI-598 had finer starting grain sizes (20 and 5 μm, respectively) and deformed mainly in the diffusion creep regime. In both experiments, the samples strengthened progressively with time, presumably because of grain growth. Further details about the experiments, rheological data and stress–strain curves are described by Bystricky (1998) and Bystricky and Mackwell (submitted).

3.3. Torsion experiments

A torsion experiment on a hot-pressed clinopyroxenite sample was performed in a Paterson gas-medium apparatus located at ETH Zürich. The torsion apparatus and technique are described by Paterson and Olgaard (2000). It has been used successfully for high shear strain experiments of

calcite (Casey et al., 1998; Pieri et al., in press a), anhydrite (Stretton and Olgaard, 1997; Heidelbach et al., submitted), quartz (Schmocker et al., 1999) and olivine (Bystricky et al., 1999).

Sample P0-228 was hot-pressed for 10 h at 1200°C and 300 MPa using coarse-grained (30 μm) diopside powder. Immediately afterwards, the sample was deformed at 1200°C and 300 MPa at constant angular displacement rate, corresponding to a constant shear strain rate of 1.1×10^{-4} s^{-1} at the outer radius of the sample. The torque recorded during the experiment yielded a shear stress of approximately 230 MPa at the outer radius assuming a constant flow law with stress exponent n of 4.7 through the whole specimen. In order to compare these data with those from the axial compression experiments, values of 6.4×10^{-5} s^{-1} and 380 MPa were derived for equivalent strain rate and stress in compression based on the Von Mises yield criteria (Paterson and Olgaard, 2000). These values correspond to conditions where dislocation creep (with $n \approx 4.7$) is expected to be the dominant deformation mechanism (Bystricky and Mackwell, submitted). After yielding, the sample deformed in an 'apparent steady state', before slip occurred at the bottom sample-spacer interface at a shear strain of $\gamma \sim 0.1$, corresponding to a
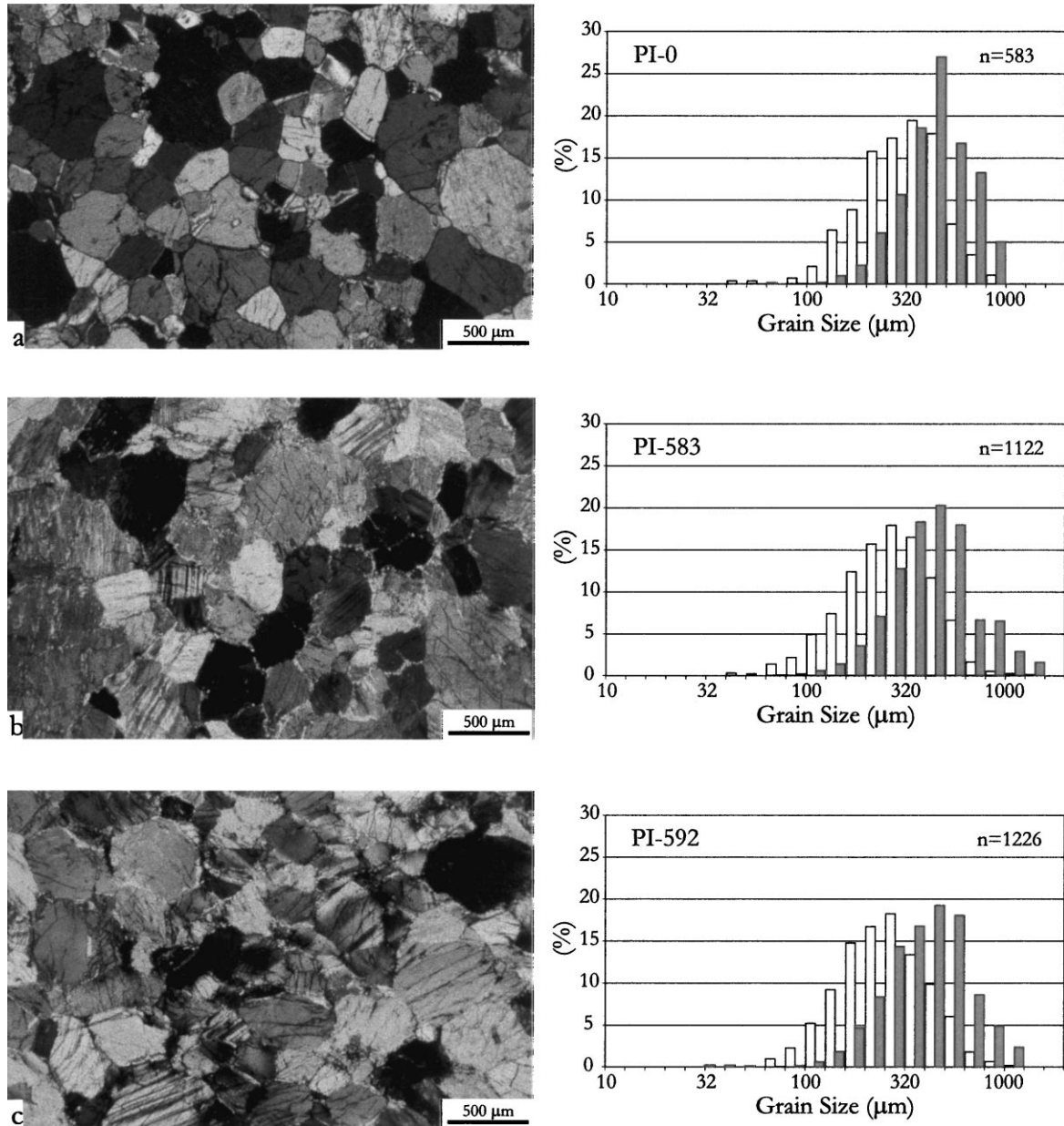
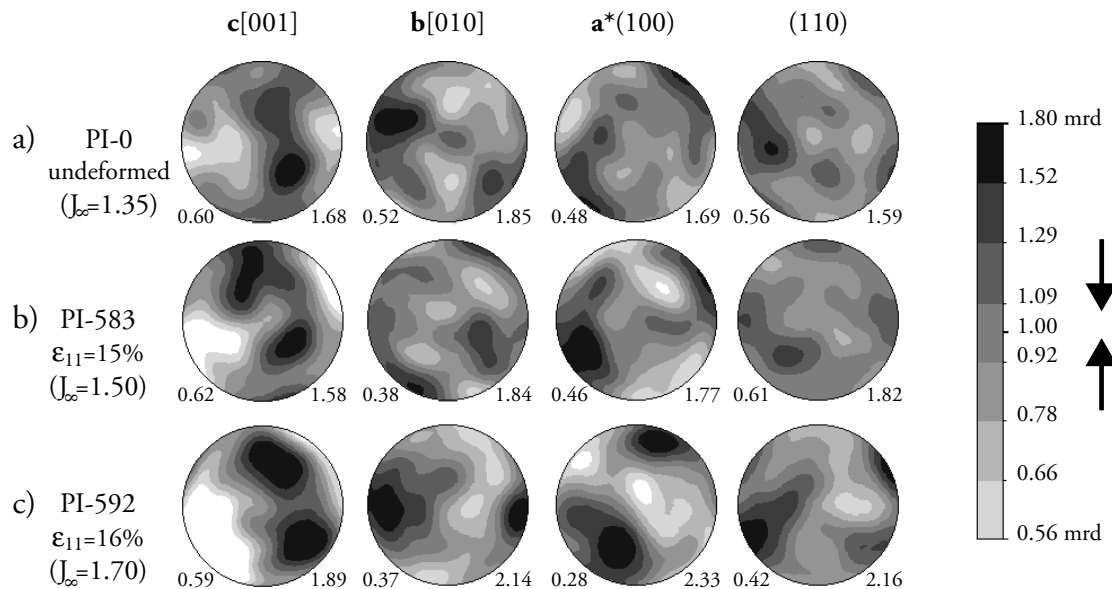Fig. 3. Microstructures of the natural samples. (a) Sample PI-0, undeformed. (b) Sample PI-583, deformed to 15% shortening. (c) Sample PI-592, deformed to 16% shortening. Left: Polarized light micrographs oriented with cylinder axis vertical. Right: Grain size histograms expressed as number fraction (white) and area fraction (grey) on a logarithmic scale.

total natural strain $\varepsilon \sim 0.05$ or an axial shortening of 5% (Ramsay and Huber, 1983).

4. Microstructures and LPO of natural clinopyroxenite

4.1. Starting material

The microstructure of the natural Sleaford Bay clinopyroxenite is well equilibrated with equiaxed grains separated by straight to slightly curved grain boundaries (Fig. 3a). A few thin, straight twins are visible. Fractures along the (110) cleavage planes are common. The average measured 2D

grain size is 330 μm (Fig. 3a) and lies between the values of 264 and 600 μm reported for samples from the same locality by Boland and Tullis (1986) and Kirby and Kronenberg (1984), respectively. The texture of the starting material was measured on a cylinder of the type used for the experiments, and is represented by pole figures of the **c**[001] and **b**[010] axes as well as **a***(100) and (110) poles with the cylinder axis vertical as indicated in Fig. 4a. The Sleaford Bay pyroxenite has a significant LPO marked by a point maximum of **b**[010] axes and a girdle of **c**[001] axes perpendicular to it. This LPO would correspond to an 'S-type' fabric with the **b**[010] maximum normal to a foliation plane. Without any macroscopic foliation visible and without a

Fig. 4. Pole figures of the natural samples. (a) Sample PI-0, undeformed. (b) Sample PI-583, deformed to 15% shortening. (c) Sample PI-592, deformed to 16% shortening. Logarithmic scale on upper hemisphere equal area projection. Diagrams are oriented with the cylinder axis vertical.

knowledge of any existing fabric, the cylinders were all cored with the cylinder axis nearly normal to the **b**[010] maximum (Fig. 4a).

4.2. Deformed samples

Microstructures of the natural samples deformed in compression are illustrated in Fig. 3b, c. In both samples, grain sizes are the same as in the starting clinopyroxenite. No pronounced shape preferred orientation has developed after strains of 16%. Evidence of intracrystalline deformation is documented by intensive undulose extinction, deformation bands and twinning. Although some of the narrow twins may have been introduced during the unloading stage of the experiments, the deformed samples contain substantially more twins than the starting material. They are either thin and bent or thick with a lensoid shape. Subgrains are not common, but when observed, their size is around 30–50 μm. Grain boundaries are generally straight at the grain scale. At a finer scale, first signs of slow grain boundary migration by bulging are visible. These observations suggest that deformation occurred mainly by mechanical twinning and dislocation glide without major amounts of recrystallization.

Pole figures for the **c**[001] and **b**[010] directions, as well as (110) and **a***(100) poles are presented for the undeformed and both deformed samples in Fig. 4, with the compression direction vertical. As compression is rotationally symmetric and as no reference was marked on the samples, thin sections were cut parallel to the compression direction but along different planes, which were not parallel in the block of natural rock. In order to present all three textures within a common sample reference frame, the fabrics were rotated around the compression axis until they were most similar.

The initial LPO pattern did not undergo strong changes during deformation. The **b**[010] axes lie nearly normal to the compression axis. A girdle of **c**[001] axes is inclined with respect to compression and the **a***(100) poles are normal to it. The LPO strength increases with progressive deformation, the point maxima of the **b**[010] and **a***(100) directions become clearer and the girdle of **c**[001] becomes more pronounced. The LPO pattern presents more internal symmetry and seems to evolve towards an orthorhombic fabric with respect to both the initial foliation plane and the compression axis. Thus, after this amount of deformation, the texture is still dominated by the initial fabric. The LPO has not yet been overprinted by the compressive deformation, which should ultimately result in an orientation distribution rotationally symmetric around the compression axis.

5. Microstructures and LPO of hot-pressed diopside aggregates

5.1. Starting material

Thin slices were cut from one end of each of the hot-pressed cylinders for microstructural analysis, while the rest of the sample was deformed. Thus, the microstructures of the undeformed hot-pressed samples were observed on sections oriented normal to the compaction axis. Although care was taken to remove optically visible impurities during specimen preparation, individual grains of quartz and apatite are present in all samples and comprise up to 5% of the sample volume based on atomic number contrast SEM images. The hot-pressed microstructures do not show foam textures. Strain features, such as twins and undulose
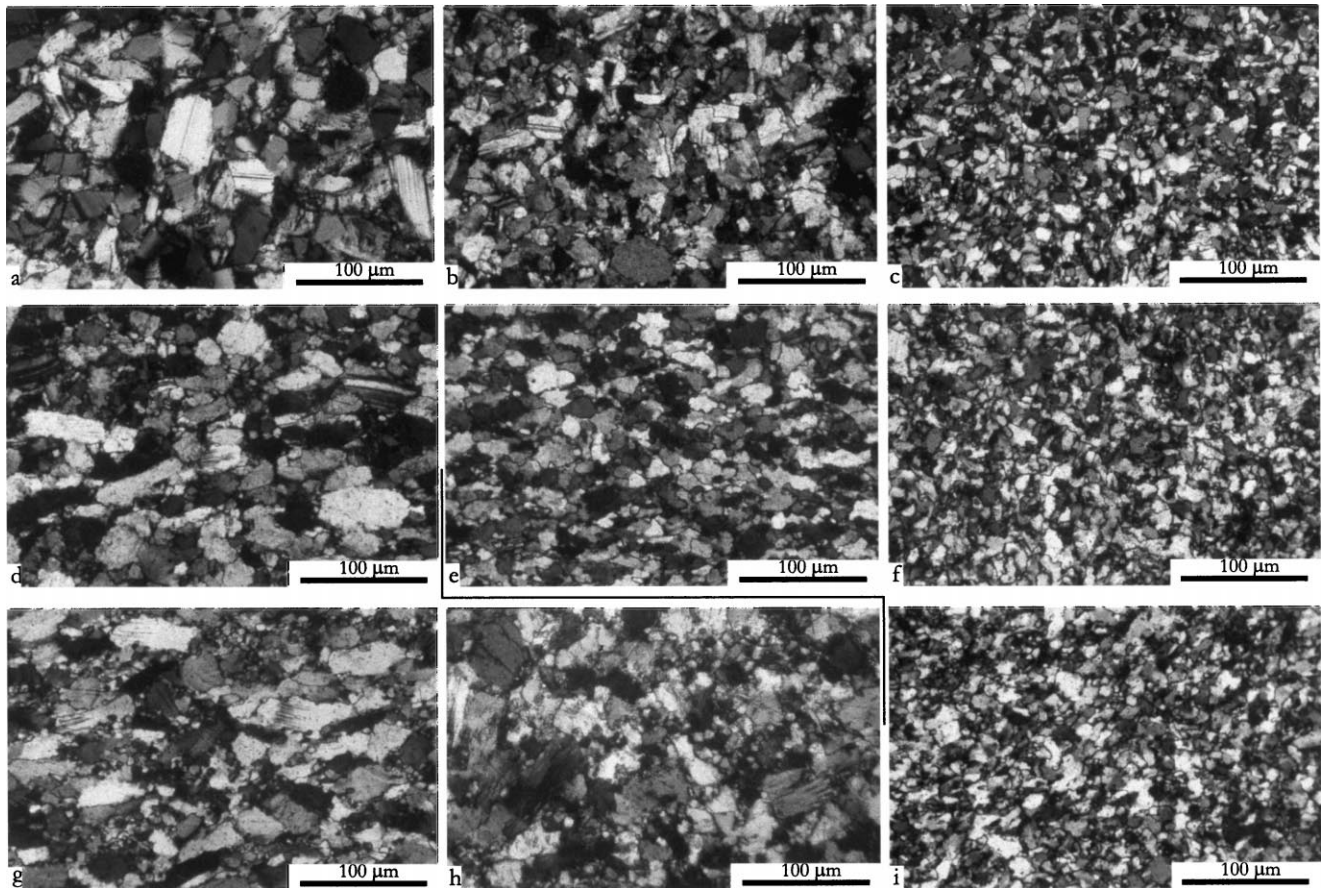
Fig. 5. Polarized light micrographs of the hot-pressed samples deformed in compression and torsion. (a) Sample HP-6, undeformed, starting grain size 30 μm. (b) Sample HP-11, undeformed, starting grain size 20 μm. (c) Sample HP-12, undeformed, starting grain size 5 μm. (d) Sample PI-527, deformed to 28% shortening. (e) Sample PI-588, deformed to 25% shortening. (f) Sample PI-598, deformed to 17% shortening (section perpendicular to compression). (g) Sample PI-528, deformed to 19% shortening. (h) Sample P0-228, deformed to $\gamma = 0.1$ in torsion. (i) Sample PI-598, deformed to 17% shortening (section parallel to compression). Sections of HP-6, HP-11 and HP-12 were cut perpendicular to the compaction direction. Sections of the deformed samples are presented with the cylinder axis vertical. For the sample deformed in torsion, the shear direction is horizontal and the sense of shear is dextral.

extinction, are visible. Grains are often elongated but are oriented randomly within the plane perpendicular to the compaction direction. Grain boundaries are mostly straight.

Microstructures were analysed for three hot-pressed samples prepared from powders with 3D grain sizes in the ranges 20–40 μm (HP-6), 10–30 μm (HP-11) and 1–10 μm (HP-12). The samples have uniform distributions of grain sizes with 2D means of 30, 20 and 5 μm, respectively (Figs. 5a–c, 6a–c). In sample HP-12, some clusters 10–100 μm in size of very fine-grained material (<1 μm) were observed, which probably agglomerated prior to and flattened during cold pressing. Similar grain clusters were not observed in the samples with larger grain sizes, where the finest-grained fractions had been removed. Grain sizes before and after hot-pressing of sample HP-11 were determined from 3D (powder) and 2D (microstructural) analysis, respectively. Comparison of the histograms indicates that there is no significant grain growth during hot-pressing (Fig. 2).

LPO measurements on sample HP-11 (Fig. 7) show a texture of moderate strength with a texture index close to 1.4. The fabric is characterized by a girdle of c[001] axes normal to the compaction direction. Pole figures of the b[010] axis, a*(100) and (110) poles all display a similar maximum concentration parallel to the compaction direction. This LPO is interpreted as a result of compaction during cold-pressing. The grains in the starting powders have an elongated shape parallel to c[001] because of the good {110} and (100) cleavage planes (Fig. 8a). Therefore grains aligned preferentially with the c[001] axis perpendicular to the compaction direction during cold-pressing. The similar distributions for the other crystal directions perpendicular to c[001], all with a maximum parallel to the compaction axis, can be explained by a so-called ring-fiber texture. Grain orientations are randomly distributed around the c[001] axis, which itself is oriented normal to and rotationally symmetric around the compaction direction (Fig. 8b). In an inverse pole figure, the compaction direction Y_s is preferentially aligned with all directions normal to c[001]. A similar but slightly weaker fabric was obtained from LPO measurements on HP-12. Since the same preparation techniques were applied and similar
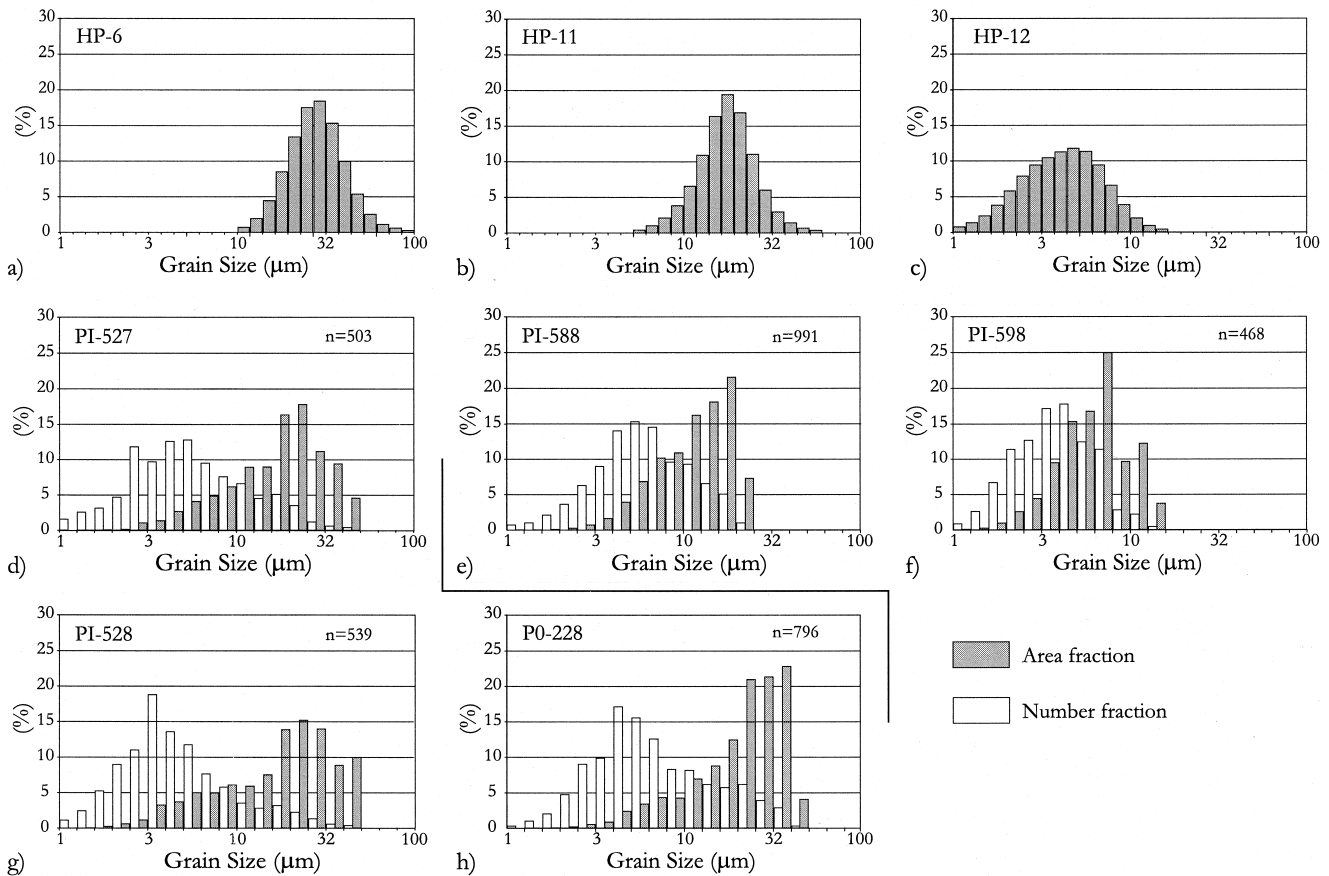
Fig. 6. Grain size histograms of the hot-pressed samples expressed as number fraction (white) and area fraction (grey) on a logarithmic scale. For the undeformed samples, the grain size was deduced from 3D powder data and is therefore given as 2D area fraction only. (a) Sample HP-6, undeformed, starting grain size 30 μm. (b) Sample HP-11, undeformed, starting grain size 20 μm. (c) Sample HP-12, undeformed, starting grain size 5 μm. (d) Sample PI-527, deformed to 28% shortening. (e) Sample PI-588, deformed to 25% shortening. (f) Sample PI-598, deformed to 17% shortening. (g) Sample PI-528, deformed to 19% shortening, (h) Sample P0-228, deformed to $\gamma = 0.1$ in torsion. Samples PI-527, PI-528 and P0-228 were prepared like HP-6, PI-588 like HP-11 and PI-598 like HP-12.

random distributions of elongated grains within the thin section normal to compaction were observed in HP-6, we infer a similar initial LPO for the coarse-grained samples.

5.2. Microstructures of the samples deformed in compression

Sample PI-527 (Fig. 5d) was hot-pressed from powder with an average 2D grain size of 30 μm and deformed to 28% shortening. The sample displays plastically deformed grains with small subgrains and recrystallized grains along the grain boundaries. A foliation is defined normal to compression by the clear shape preferred orientation of the elongated grains. Deformation features include twins, deformation bands and undulose extinction. Some of the generally thick twins are bent, while others are either pinned at the grain boundaries or have a tapering edge. Slow grain boundary migration can be recognized by curved to lobate boundaries in the deformed grains as well as by some 'left-over' grains. The area fraction of recrystallized grains is extracted from the grain size histogram (Fig. 6d) by the

percentage of grains with sizes below 8 μm. This limit was chosen at the lower bound of the initial size distribution to exclude the old grains. The recrystallized grains represent around 15% of the area with a peak frequency around 5 μm.

Sample PI-528 (Fig. 5g), hot-pressed from powder with an average 2D grain size of 30 μm, was deformed to 19% shortening at a higher differential stress than the previous sample. It exhibits a microstructure representative of intra-crystalline deformation accommodated by subgrain rotation recrystallization. Twins, deformation bands and subgrains are frequent. Serrated and dentate grain boundaries are numerous. A foliation normal to compression is defined by the shape preferred orientation of the larger elongated grains but is less pronounced than in PI-527. Recrystalliza-tion is more evident from numerous small recrystallized grains around the deformed grains in a core-and-mantle structure. The area fraction of recrystallized grains, as given by the grain size histogram, is around 20% with a peak frequency around 3 μm, which is finer than in PI-527, presumably because of the higher differential stress sustained by the sample (Fig. 6g).
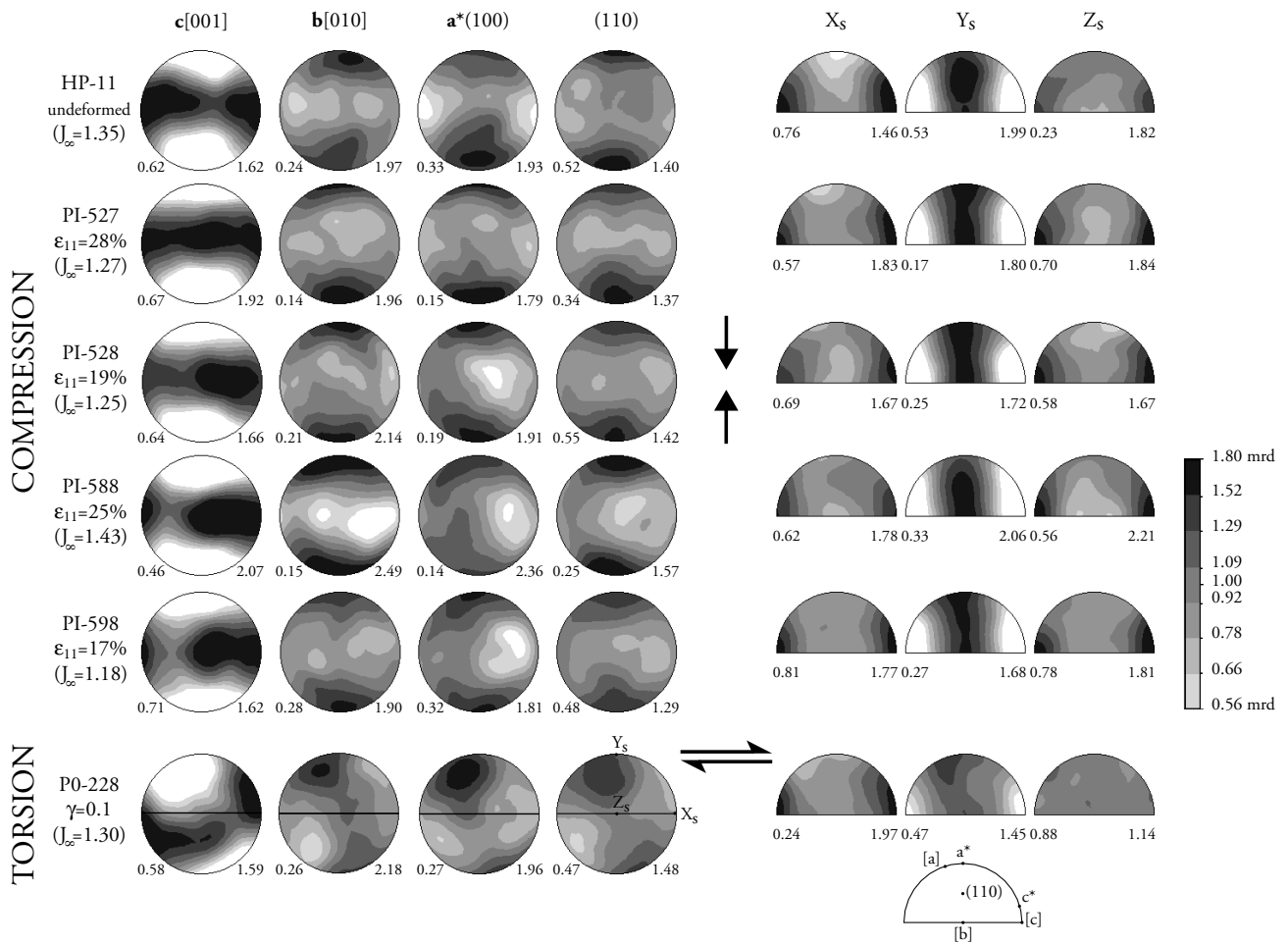
Fig. 7. Pole figures (right) and inverse pole figures (left) of the hot-pressed samples on a logarithmic scale on upper hemisphere equal area projection. All figures were reduced by the inversion symmetry, minimum and maximum intensities (times random) are given below each figure. Pole figures are oriented with the cylinder axis vertical. For the sample deformed in torsion, the shear direction is horizontal with dextral sense of shear. For inverse pole figures, a reference key is given with crystallographic directions. For the samples deformed in compression, Y_s is parallel to the compression axis and X_s and Z_s are normal to it. For the sample deformed in torsion, X_s corresponds to the shear direction and Y_s to the shear plane normal.
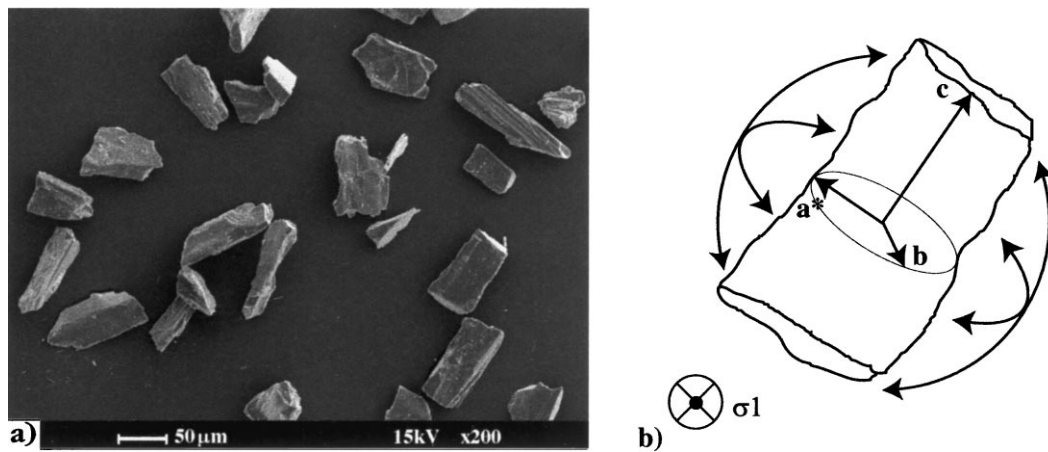
Fig. 8. Origin of the initial fabric during cold-pressing. (a) Secondary electron image of crushed powder used for generation of the synthetic material. Note the elongated grain shapes parallel to the **c**[001] axis. (b) Schematic distribution of the crystallographic axes of diopside grains producing a ring-fiber texture. The **c**[001] axes fall randomly within the viewed plane. For each orientation of the **c**[001] axis, the **b**[010] and **a***(100) directions are randomly distributed normal to **c**[001].

Sample PI-588 (Fig. 5e) was hot-pressed from powder with an average 2D grain size of 20 μm and deformed to 25% shortening. Grains have a slight elongation with a shape preferred orientation that defines a weak foliation normal to compression. Deformation twins are rare, and deformation bands and undulose extinction are less pronounced than in the coarse-grained samples. Subgrains are more common. Small, equant grains with a similar size (4–8 μm) as in sample PI-527 have developed by dynamic recrystallization. The proportion of small recrystallized grains is slightly larger with an area fraction of 25%, even though it includes a minor fraction of grains initially smaller than 8 μm. Grain boundaries are irregular, from lobate to serrated, and show bulging. The mechanical data indicated some strengthening with time, which was previously interpreted as resulting from grain growth during creep at 1200°C. However, our measurements indicate that the average grain size was reduced, and there are no grains significantly larger than in the starting material (Fig. 6e).

Sample PI-598 was hot-pressed from powder with an average 2D grain size of 5 μm and was deformed to 17% shortening predominantly in the diffusion creep regime. The sample exhibits a homogeneous grain size of 2–12 μm. Grains can be described as nearly strain-free, although minor undulose extinction is visible (Fig. 5f, i). The grain boundaries are highly inhomogeneous from straight through slightly curved to highly serrated, indicating diffusion creep with mobile grain boundaries as opposed to grain boundary sliding, which would be represented by mainly straight grain boundaries. A weak foliation is defined by slightly elongated diopside grains normal to compression and underlined by flattened clusters of the very fine-grained agglomerates. For this sample, the mechanical data indicated even more strengthening than PI-588 during creep at 1200°C. Optically, no clear difference in grain size is visible between the undeformed sample HP-12 and either of the two perpendicular sections of the deformed sample PI-598 (Fig. 5c, f, i). Histograms indicate a small increase in grain size during the experiment from HP-12 to PI-598 (Fig. 6c, f). The hardening due to the apparent increase in grain size by a factor of ∼1.5 would correspond to a decrease in strain rate by a factor of $1.5^2 \sim 2.2$ or $1.5^3 \sim 3.4$ based on a Nabarro–Herring or a Coble creep flow law, respectively. The hardening observed during deformation of this sample lies well within this range (Bystricky, 1998).

5.3. LPO of the samples deformed in compression

All of the hot-pressed samples show the same overall texture (Fig. 7), which was already present in the starting material. It is defined by a ring-fiber texture with a girdle of **c**[001] axes normal to the compression direction. Pole figures of the **b**[010] axis, **a***(100) and (110) poles display maximum concentrations parallel to the compression direction. In the inverse pole figures, the compression direction Y_s is aligned with a girdle normal to **c**[001]. This girdle is very pronounced in all the samples, except in sample PI-588 where the maximum close to **a***(100) is reduced. The rotational symmetry about the compression axis is followed reasonably well in all the samples, as the inverse pole figures of the two directions X_s and Z_s normal to compression are similar with a concentration parallel to **c**[001].

The extrapolated texture index varies slightly from one sample to another (Table 1). For the three samples deformed by dislocation creep and partially recrystallized, the texture strength decreased slightly for PI-527 and PI-528, while it increased for PI-588 compared to the initial LPO (HP-11). The texture strength seems to be rather insensitive to the amount of finite strain (PI-527 was deformed to the highest strain) but sensitive to the amount of recrystallization (PI-588 was most recrystallized). For the fine-grained samples (HP-12 and PI-598), the LPO is similar to but weaker than that of the coarser-grained material. Deformation by diffusion creep did not visibly alter the initial LPO.

5.4. Sample deformed in torsion

Sample P0-228 (Fig. 5h) was hot-pressed from powder with an average 2D grain size of 30 μm and deformed to $\gamma = 0.1$ in torsion. The microstructure shows large elongated grains, which are surrounded by small and equant recrystallized grains. The aspect ratio of the larger grains represents their initial shape. A weak oblique foliation is defined at about 35° from the shear zone boundary by the elongated grains. Evidence for intracrystalline deformation includes the presence of twins, deformation bands, undulose extinction and subgrains. Grain boundaries are often lobate to serrated. Newly recrystallized grains, 3–8 μm in size, constitute around 20% of the sample area as determined from the grain size histogram (Fig. 6h). They form a core-and-mantle structure with the relict grains, which is characteristic for subgrain rotation recrystallization.

The LPO of this sample has evolved from the initial axial symmetric compaction texture towards a texture with a girdle of **c**[001] axes inclined opposite to the sense of shear. The other directions concentrate in point maxima normal to this girdle. The overall fabric displays a monoclinic texture symmetry as should arise from the shear deformation in torsion experiments. However, the corresponding two-fold symmetry axis is not exactly in the center of the pole figures, but about 15° off the shear plane. Misalignments of the section cut with respect to the torsion axis can only explain a small part (about 2°) of this observed deviation, while the origin of most of the deviation remains unknown. On the inverse pole figure, the shear plane normal Y_s defines a girdle normal to **c***(001), with a small maximum close to **a**[100]. The shear direction X_s aligns close to **c**[001]. The texture index is similar to the one of the starting fabric.

5.5. LPO of recrystallized grains

Lattice orientations of recrystallized grains were separated

from the bulk texture on a fine-scale orientation map with a step size of 2 μm for sample PI-588 (Fig. 9). Colors are attributed to the measurements on the map as well as on separate pole figures according to the measured grain size. No postprocessing was applied to the acquired orientation maps. In the smallest grain size fraction (2.3 μm, equivalent to 1 pixel), unreliable measurements with CI < 0.2 probably correspond to weak EBSD patterns obtained on grain boundaries, impurities or surface artifacts. They form about 9% of the total data and have random orientations. Reliable orientations with CI > 0.2 in the same size fraction originate from recrystallized diopside grains with a size below 3.2 μm (2 pixels). In the larger grain size fractions, orientations with low reliability (CI < 0.2) were not separated as they are too few to influence the overall texture.

In sample PI-588, recrystallized grains were defined by a grain size below 8 μm, as suggested above based on grain size histograms. The LPO of the recrystallized grains is characterized by a girdle of **c**[001] axes normal to compression, a point maximum of **b**[010] parallel to compression and a random distribution of **a***(100). In the inverse pole figures, the compression direction Y_s is aligned to the **b**[010] axis and less pronounced with a girdle normal to **c**[001]. Grains with a size between 8 and 10 μm have a similar fabric although some asymmetry relative to the compression axis is visible. For the larger grains (above 10 μm), the **c**[001] axes form a wide point maximum within the foliation. The **a***(100) poles tend to be aligned parallel to the compression direction in the same way as the **b**[010] axes. In the inverse pole figures, the compression direction Y_s shows a weak preferred orientation along a girdle normal to **c**[001]. With increasing grain size, the number of measured grains becomes rather small and less representative. Clusters of grains aggregated with similar lattice orientations during cold-pressing and are responsible for deviations from a rotational symmetry in the LPO of the coarse size fractions.

No principal texture transition was observed between initial and recrystallized grains in the **b**[010] and **c**[001] pole figures. A transition is visible for the **a***(100) poles from a preferred alignment parallel to the compaction axis Y_s in the coarse grains to a more random distribution in the fine recrystallized fraction. The ring-fiber texture of the starting material is replaced by a common S-type fabric in the recrystallized grains.

6. Discussion

This study presents a detailed analysis of microstructures and LPO of experimentally deformed clinopyroxene aggregates. Coarse-grained natural samples, deformed in compression up to 16% shortening, display microstructures representative of deformation by mechanical twinning and dislocation glide. These observations are consistent with the

measured non-linear viscous flow law with a stress exponent $n = 4.7$ (Bystricky and Mackwell, submitted) interpreted as due to dislocation creep.

Hot-pressed samples were deformed near the transition between dislocation and diffusion creep. Four samples deformed mainly in the dislocation creep regime during axial compression (PI-527, PI-528, PI-588) and during the torsion test (P0-228). Dislocation creep was accompanied by dynamic recrystallization through subgrain rotation and slow grain boundary migration. The area fraction of recrystallized grains varies from 10 to 25% in the different samples. The observed size and fraction of dynamically recrystallized grains appear to respond to the applied differential stresses. No general correlation between the extent of recrystallization and the texture strength could be established.

The textures of the hot-pressed samples differ from the ones reported by Carter et al. (1972) from experiments in axial compression on hot-pressed diopside aggregates performed at low strain rate (8×10^{-7} s^{-1}) in a Griggs solid-medium apparatus. In our study, **b**[010], **a***(100) and therefore **a**[100] align parallel to σ_1, while **c**[001] forms a girdle in the $\sigma_2 = \sigma_3$ plane. Carter et al. (1972) reported an S-type fabric where only **b**[010] aligns parallel to σ_1, and **a**[100] and **c**[001] form girdles in the $\sigma_2 = \sigma_3$ plane. They did not describe the initial fabric prior to deformation, but observed significant grain growth during the deformation, suggesting that the microstructure equilibrated and that a growth fabric was produced. Consequently, the fabrics in our axial compression samples should evolve towards a similar S-type pattern with increasing strain and time as visible in the recrystallized grain fraction of sample PI-588, where the point maximum of **a***(100) vanished.

It is important to know whether the LPO of the deformed samples is only due to compaction during cold pressing or results from a combination of both the initial fabric and intracrystalline deformation. In the natural samples, we observed that after 16% shortening the initial texture incipiently evolved to a new texture presumably imposed by the active slip systems. By contrast, deformation of the hot-pressed samples resulted in only minor changes in texture. For these samples, the fabric obtained after cold-pressing may not be very different from that which develops during deformation by axial compression. For dominant glide on a single slip system, the 'easy slip' plane as well as the 'easy slip' direction should align normal to the compression direction (Schmid, 1982; Wenk and Christie, 1991). Here, the **a***(100), **b***(010) and (110) planes are oriented normal to compression as potential slip planes, with **c**[001] as the slip direction. With the rotational symmetry of the deformation, an equal activation of all the systems {hk0} **c**[001] could explain the fabric. From symmetry considerations, the compaction fabric is described by a ring-fiber texture, which is rotationally symmetric both about the sample axis Y_s and about the crystal axis **c**[001]. Any resulting compression fabric should stay rotationally symmetric
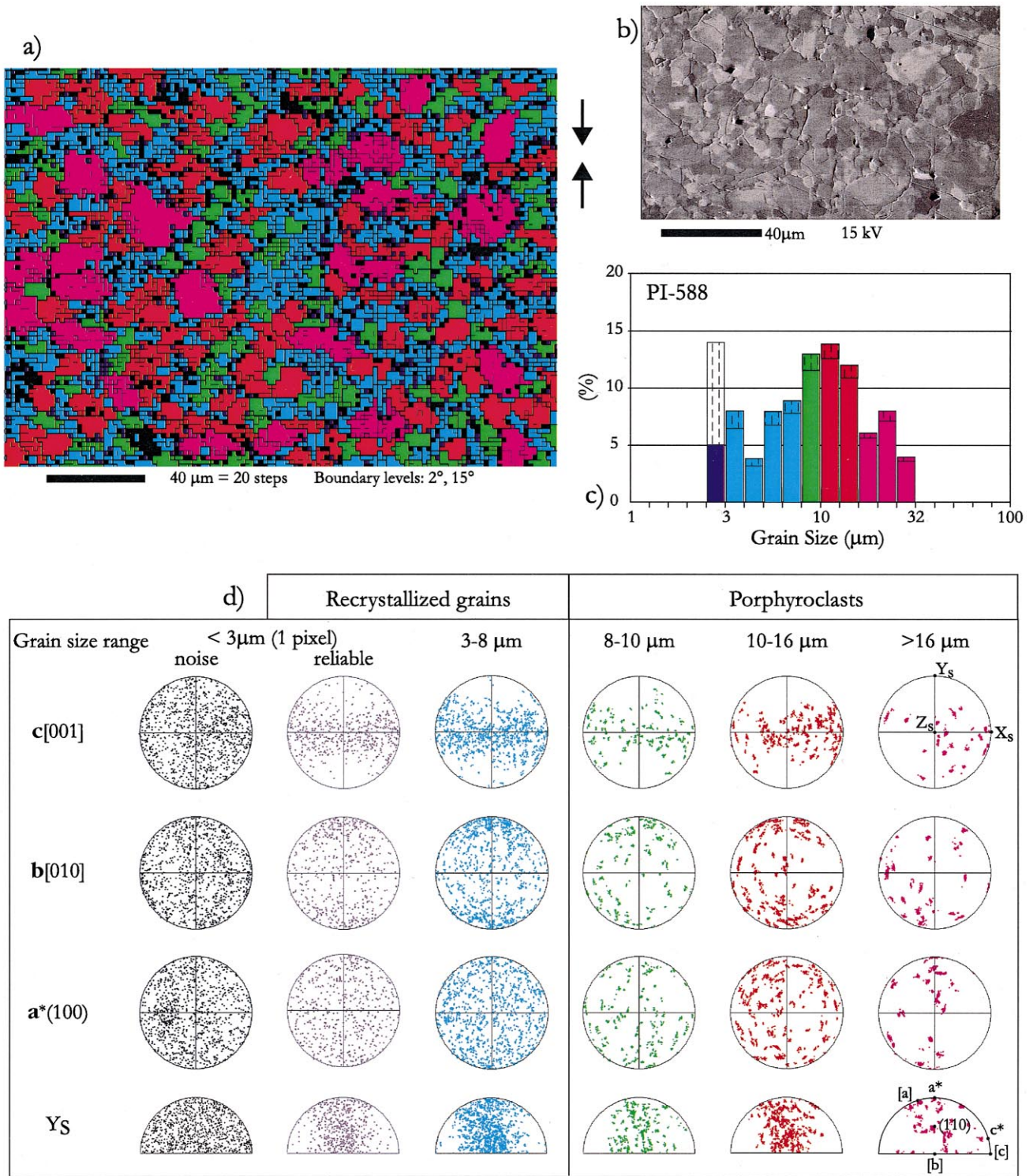
Fig. 9. Fabric variation with grain size in sample PI-588. (a) OIM map with a step size of 2 μm. Grains are defined as groups of connected measurements whose neighbor to neighbor misorientations do not exceed 15°. They are highlighted according to their size and confidence index (CI): grains with a size < 3 μm (1 pixel) and CI < 0.2 (black), < 3 μm and CI > 0.2 (dark blue), 3–8 μm (light blue), 8–10 μm (green), 10–16 μm (red), > 16 μm (pink). Grain boundaries (misorientation angle > 15°) are marked by thick lines and subgrain boundaries (misorientation angle > 2° and < 15°) by thin lines. (b) SEM orientation contrast image showing newly recrystallized fine grains, old coarse grains and surface artifacts. (c) Grain size histogram deduced from OIM measurements. Color coding as used in the OIM map. Fractions with CI < 0.2 are striped. (d) Pole figures for **c**[001], **b**[010], **a***(100) and inverse pole figure for the compression direction Y_s for the different grain size fractions as defined above.

{110} 1/2 <a±b>   (100) **c**[001]   (010) **a**[100]

{110} **c**[001]   (100) **b**[010]   (010) [a±c]
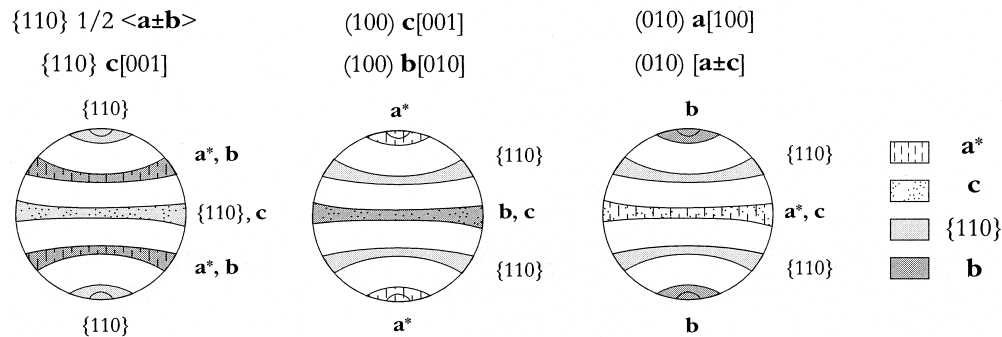
Fig. 10. Schematic pole diagrams of hypothetical fabrics, which would develop during compression of clinopyroxene assuming exclusive activation of one single slip system as indicated. Regardless of the slip direction, the slip plane is preferentially oriented normal to the compression axis. LPO patterns of the **c**[001] axis (dotted), **b**[010] axis (dark grey), **a***(010) pole (striped) and (110) pole (light grey) are presented.

about the loading axis. However, it will preferentially align some distinct lattice planes normal to the compression direction while the rotational symmetry about **c**[001] will vanish, forming a conventional fiber texture. For all the reported slip systems on {110}, (100) and (010), the hypothetical 'easy slip' fabrics are schematically drawn in Fig. 10 with the respective slip planes oriented normal to the compression axis. At the high temperatures applied here, the {110} slip planes are most favored. Therefore one should see a trend to strengthen the {110} maximum towards the compression direction, which starts to be visible for PI-588. In summary, the observed fabrics are at the beginning of the expected transition from the initial ring-fiber texture to a conventional fiber texture similar to an S-type fabric in natural pyroxenites.

In the majority of previous experimental studies on LPO evolution, a random starting texture was generally implied, and the resulting fabrics were assumed to have reached steady state. Rutter et al. (1994) showed that calcite develops a LPO also during deformation in the grain-size sensitive regime, and that a pre-existing fabric is preserved during such deformation. They concluded that large strains are required to overprint an existing LPO. High strains are also necessary to evolve from a transient deformation texture to a steady-state microstructure in stationary equilibrium between intracrystalline deformation and recrystallization (Pieri et al., in press b). Thus we believe that the amount of strain applied in our compression experiments was not enough to significantly alter the initial compaction fabric.

The fine-grained sample (PI-598) shows evidence of grain boundary migration and grain growth. In this sample, the resulting fabric is as weak as the initial fabric, suggesting that diffusional processes were competitive with intracrystalline deformation. This is consistent with the determined linear viscous flow law (Bystricky, 1998).

Torsion deformation (P0-228) produced a monoclinic fabric oblique with respect to the shear plane and shear direction that is still dominated by the rotationally symmetric fabric developed during cold-pressing. It is likely that such shear fabric is transient for moderate shear strains

before it will be replaced by a recrystallization fabric at shear strains γ above 1 to 5, as reported for norcamphor (Herwegh et al., 1997), calcite (Pieri et al., in press b) and olivine (Bystricky et al., 1999). This working hypothesis underlines the need for further experimental and textural studies on pyroxenes to be extended to high strain deformation. By deforming samples to higher strain in a different geometry than during synthesis, such experiments should isolate the effects of a starting LPO. Torsion experiments to high strain and under constant load may reach a steady-state microstructure and LPO, and therefore provide further information about deformation mechanisms in clinopyroxene.

7. Summary and conclusions

Microstructures and LPO were investigated in clinopyroxenes aggregates deformed in compression and torsion, leading to the following conclusions:

1. Under the conditions investigated, coarse-grained clinopyroxenite deformed mainly by twinning and dislocation glide. Because of a starting fabric and the amount of strain achieved, no clear fabric evolution could be followed.
2. In hot-pressed samples deformed within the dislocation creep regime, dynamic recrystallization occurred mainly by subgrain rotation, but also by slow grain boundary migration. With reduced initial grain size, grain boundary mobility increased.
3. Uniaxial cold-pressing of clinopyroxene aggregates generates a significant LPO in the samples prior to deformation due to a preferred shape of the powder crystals. Thus, proper care must be taken when assuming a random LPO in synthetic as well as natural rocks.
4. Large strains (at least more than 25% shortening as applied here) are necessary to overprint a pre-existing LPO in clinopyroxenes and to recrystallize a major proportion of the sample. Deformation both in the dislocation creep and diffusion creep regimes does not rapidly

alter the initial LPO. Newly recrystallized grains develop a different fabric which respects the kinematic framework of the deformation.

5. Deformation in torsion to a shear strain of $\gamma = 0.1$ generates a fabric oblique to the shear plane and shear direction, which is probably transient. Higher strain torsion experiments have to be performed to reach steady-state microstructures and LPO in clinopyroxene.

Acknowledgements

References

Adams, B.L., Wright, S.I., Kunze, K., 1993. Orientation imaging: the emergence of a new microscopy. Metallurgical Transactions 24A (4), 819–830.

Avé Lallemant, H.G., 1978. Experimental deformation of diopside and websterite. Tectonophysics 48, 1–27.

Boland, J.N., Tullis, T.E., 1986. Deformation behavior of wet and dry clinopyroxenite in the brittle to ductile transition region. Mineral and Rock Deformation: Laboratories Studies. The Paterson Volume. Geophysical Monograph 36, 35–49.

Brenker, F.E., 1998. Mikrogefügethermochronometrie für Eklogite. Ph.D. thesis. J.W. Goethe Universität, Frankfurt am Main.

Brenker, F.E., Prior, D.J., Müller, W.F., 1999. Cation ordering in omphacite and effect on deformation mechanism and lattice preferred orientation. In: Dresen, G., Handy, M., Janssen, C. (Eds.), International Conference on Deformation Mechanisms, Rheology and Microstructures, Neustadt an der Weinstrasse, p. 11.

Bunge, H.J., 1982. Texture Analysis in Materials Science—Mathematical Methods. Butterworths, London.

Bystricky, M., 1998. High temperature deformation of clinopyroxene and clinopyroxene-plagioclase aggregates. Ph.D. thesis, Pennsylvania State University.

Bystricky, M., Kunze, K., Burlini, L., Burg, J.-P., 1999. Rheology and texture of olivine aggregates deformed to high strains in torsion. Eos Transactions. American Geophysical Union 80 (46), F973.

Bystricky, M., Mackwell, S. (submitted). Creep of dry natural and resynthesized clinopyroxenite. Journal of Geophysical Research.

Carter, N.L., Baker, D.W., George, R.P., 1972. Seismic anisotropy, flow and constitution of the upper mantle. In: Flow and Fracture of Rocks. The Griggs Volume. Geophysical Monograph 16, 167–190.

Casey, M., Kunze, K., Olgaard, D.L., 1998. Texture of Solnhofen limestone deformed to high strains in torsion. Journal of Structural Geology 20, 255–267.

Dell'Angelo, L.N., Tullis, J., 1986. A comparison of quartz c-axis preferred orientations in experimentally deformed aplites and quartzites. Journal of Structural Geology 8, 683–692.

Etheridge, C.A., Kirby, S.H., 1977. Experimental deformation of rock-forming pyroxenes: recrystallisation mechanisms and preferred orientation development. Eos Transactions. American Geophysical Union 58, 513.

Fliervoet, T.F., Drury, M.R., Chopra, P.N., 1999. Crystallographic preferred orientations and misorientations in some olivine rocks deformed by diffusion or dislocation creep. Tectonophysics 303, 1–27.

Godard, G., Van Roermund, H.L.M., 1995. Deformation-induced clinopyroxene fabrics from eclogites. Journal of Structural Geology 17, 1425–1443.

Heidelbach, F., Stretton, I.C., Kunze, K. (submitted). Texture development of polycrystalline anhydrite experimentally deformed in torsion. Geologische Rundschau.

Helmstaedt, H., Anderson, O.L., Gavasci, A.T., 1972. Petrofabric studies of eclogite, spinel–websterite and spinel–lherzolith xenoliths from kimberlite-bearing breccia pipes in south-eastern Utah and north-eastern Arizona. Journal of Geophysical Research 77, 4350–4365.

Herwegh, M., Handy, M.R., Heilbronner, R., 1997. Temperature- and strain-rate-dependent microfabric evolution in monomineralic mylonite: evidence from in situ deformation of norcamphor. Tectonophysics 280, 83–106.

Ingrin, J., Doukhan, N., Doukhan, J.-C., 1991. High-temperature deformation of diopside single crystal, 2. TEM investigation of the induced defect microstructures. Journal of Geophysical Research 96, 14287–14297.

Ingrin, J., Doukhan, N., Doukhan, J.-C., 1992. Dislocation glide systems in diopside single crystals deformed at 800–900°C. European Journal of Mineralogy 4, 1291–1302.

Kirby, S.H., Christie, J.M., 1977. Mechanical twinning in diopside $Ca(Mg,Fe)Si_2O_6$: structural mechanism and associated crystal detects. Physics and Chemistry of Minerals 1, 137–163.

Kirby, S.H., Kronenberg, A.K., 1984. Deformation of clinopyroxenite: evidence for a transition in flow mechanisms and semibrittle behavior. Journal of Geophysical Research 89, 3177–3192.

Kollé, J.J., Blacic, J.D., 1983. Deformation of single-crystal clinopyroxenites: 2. Dislocation-controlled flow processes in hedenbergite. Journal of Geophysical Research 88, 2381–2393.

Kunze, K., Wright, S.I., Adams, B.L., Dingley, D.J., 1993. Advances in automatic EBSP single orientation measurements. Textures and Microstructures 20, 41–54.

Matthies, S., Wagner, F., 1996. On the 1/n law in texture related to single crystal orientation analysis. Physica Status Solidi B196, K11–K15.

Mauler, A., 2000. Texture and microstructures in eclogites. Electron back-scatter diffraction applied to samples from nature and experiment. Ph.D. thesis, ETH Zurich.

Mauler, A., Kunze, K., Burg, J.P., Philippot, P., 1998. Identification of EBSD patterns in a monoclinic solid-state solution series: example of omphacite. Material Science Forum 275, 705–710.

Paterson, M.S., Olgaard, D.L., 2000. Rock deformation tests to large shear strains in torsion. Journal of Structural Geology 22, 1341–1358.

Pieri, M., Burlini, L., Kunze, K., Olgaard, D., Stretton, I.C. (in press). Dynamic recrystallization of Carrara marble during high temperature torsion experiments. Journal of Structural Geology.

Pieri, M., Stretton, I.C., Kunze, K., Burlini, L., Olgaard, D., Burg, J.-P., Wenk, R.H. (in press). Texture development in calcite through deformation and dynamic recrystallization during torsion to large strains. Tectonophysics.

Prior, D.J., Trimby, P.W., Weber, U.D., Dingley, D.J., 1996. Orientation contrast imaging of microstructures in rocks using forescatter detectors in the scanning electron microscope. Mineralogical Magazine 60, 859–869.

Raleigh, C.B., Talbot, J.L., 1967. Mechanical twinning in naturally and experimentally deformed diopside. American Journal of Science 265, 151–165.

Ramsay, J.G., Huber, M., 1983. The Techniques of Modern Structural Geology. Strain Analysis, 1. Academic Press, London.

Raterron, P., Doukhan, N., Jaoul, O., Doukhan, J.-C., 1994. High temperature deformation of diopside IV: predominance of {110} glide above 1000°C. Physics of the Earth and Planetary Interiors 82, 209–222.

Rutter, E.H., Casey, M., Burlini, L., 1994. Preferred crystallographic

orientation during the plastic and superplastic flow of calcite rocks. Journal of Structural Geology 16, 1431–1436.

Schmid, S.M., 1982. Microfabric studies as indicators of deformation mechanisms and flow laws operative in mountain building. In: Hsu, K.J. (Ed.) Mountain Building Processes. Academic Press, London, pp. 95–110.

Schmid, S.M., Paterson, M.S., Boland, J.N., 1980. High temperature flow and dynamic recrystallization in Carrara marble. Tectonophysics 43, 257–291.

Schmocker, M., Burlini, L, Bystricky, M., Kunze, K., Heidelbach, F., Burg, J.-P., 1999. Rheology and texture of polycrystalline quartz deformed to large strains in torsion. EOS Transactions. American Geophysical Union 80 (46), F1053.

Stretton, I.C., Olgaard, D.L., 1997. A transition in deformation mechanism through dynamic recrystallization—evidence from high strain, high temperature torsion tests. Eos Transactions. American Geophysical Union 78 (64), F723.

Underwood, E.E. 1970. Quantitative Stereology. Addison-Wesley, Reading, MA.

Venables, J.A., Harland, C.J., 1973. Electron back-scattering patterns—a new technique for obtaining crystallographic information in the scanning electron microscope. Philosophical Magazine 27, 1193–1200.

Viola, G., 2000. Kinematics and timing of the periadriatic fault system in the Giudicarie region (central-eastern Alps). Ph.D. thesis, ETH Zurich.

Wenk, H.R., 1985. Carbonates. In: Wenk, H.R. (Ed.), Preferred Orientation in Deformed Metals and Rocks; An Introduction to Modern Texture Analysis. Academic Press, Orlando, FL, pp. 361–384.

Wenk, H.R., Christie, J.M., 1991. Comments on the interpretation of deformation textures in rocks. Journal of Structural Geology 13, 1091–1110.

Wenk, H.R., Matthies, S., Donovan, J., Chateigner, D., 1998. BEARTEX: a Windows-based program system for quantitative texture analysis. Journal of Applied Crystallography 31, 262–269.